Acta Astronautica 126 (2016) 229–242

Contents lists available at ScienceDirect

Acta Astronautica

journal homepage: www.elsevier.com/locate/aa

Control of flow separation on a contour bump by jets in a Mach 1.9 free-stream: An experimental study

Kin Hing Lo *, Hossein Zare-Behtash, Konstantinos Kontis

University of Glasgow, School of Engineering, University Avenue, G12 8QQ, UK

ARTICLE INFO

Article history:
Received 14 December 2015
Accepted 12 April 2016
Available online 28 April 2016

Keywords:
Contour bump
Active jet
Supersonic free-stream

ABSTRACT

Flow separation control over a three-dimensional contour bump using jet in a Mach 1.9 supersonic free-stream has been experimentally investigated using a transonic/supersonic wind tunnel. Jet total pressure in the range of 0–4 bar was blowing at the valley of the contour bump. Schlieren photography, surface oil flow visualisation and particle image velocimetry measurements were employed for flow visualisation and diagnostics. Experimental results show that blowing jet at the valley of the contour bump can hinder the formation and distort the spanwise vortices. The blowing jet can also reduce the extent of flow separation appears downstream of the bump crest. It was observed that this approach of flow control is more effective when high jet total pressure is employed. It is believed that a pressure gradient is generated as a result of the interaction between the flow downstream of the bump crest and the jet induced shock leads to the downwards flow motion around the bump valley.

1. Introduction

Research on two- and three-dimensional contour bumps is an active research topic in the aerospace sector because of their applicability in both transonic and supersonic vehicles. Studies on wave drag reduction using contour bumps in transonic aircraft wings have been well documented in the literature [1–14]. It was found that around 10 to 20% of wave drag reduction could be achieved by using this flow control strategy. In addition, NASA proposed the concept of the Diverterless Supersonic Inlet (DSI) which implemented three-dimensional contour bumps as part of the supersonic inlet in 1950s [15]. Later studies concluded that compared to the other conventional supersonic inlet configurations, DSI could achieve higher total pressure recovery and lower flow distortion in supersonic speeds [16–20]. The results from these studies eventually materialised and DSI was first implemented into the engines of the Lockheed-Martin F-35 Lightning supersonic fighter aircraft [21].

Although using contour bumps could provide desire performance in drag reduction and high total pressure recovery in transonic and supersonic aircraft, it is known that adverse effects can be induced by flow separation and spanwise vortices formation appear downstream of the bump crest of the bumps [3,14,17]. As a result, it is important to investigate the flow separation characteristics of contour bumps in order to have better understanding in the physics of bump flow. Surprisingly, only a few studies have been conducted in this area for both subsonic and supersonic speeds. Although the subject matter of the present study is contour bump flow separation control in supersonic speed, some background information about the flow physics of contour bumps in subsonic free-stream is also included to provide a more complete literature survey.

In subsonic flow, Byun [22] and Byun et al. [23] investigated experimentally the formation of spanwise vortices downstream of the bump crest for a range of three-dimensional rounded contour bumps. The authors concluded that the number and size of the spanwise vortices that formed depended on the width and apex height of the bump. In addition, large-scale three-dimensional flow structures were observed which indicated the presence of a wake region downstream of the bump crest. Recently, Yakeno et al. [24] numerically investigated the streamwise flow pattern over a two-dimensional rounded contour bump in laminar flow. The results obtained suggest that flow separation appears immediately downstream of the bump crest which leads to the formation of three-dimensional flow structures in the wake region. The authors found that their size and shape depend on the Reynolds number of the flow and a similar conclusion was also drawn by Iaccarino et al. [25] in turbulent flow.

Lo [26], Lo and Kontis [27] and Lo et al. [28,29] investigated experimentally the flow pattern around a three-dimensional rounded contour bump in both Mach no. 1.3 and 1.9 supersonic free-stream. Experimental data showed that flow separation did appear immediately downstream of the bump crest which led to the formation of a large wake region. In addition, the authors in these studies showed that counter-rotating spanwise vortices were formed in the bump valley which is agreed with the finding obtained by Konig et al.

* Corresponding author.
E-mail addresses: kinhing.lo@glasgow.ac.uk (K.H. Lo), hossein.zare-behtash@glasgow.ac.uk (H. Zare-Behtash), kostas.kontis@glasgow.ac.uk (K. Kontis).

http://dx.doi.org/10.1016/j.actaastro.2016.04.033
0094-5765/

[3]. In addition, the results shown in these studies suggested that the size of the wake region and spanwise vortex pairs that formed downstream of the bump crest decreased when the free-stream Mach number was increased from $M_\infty = 1.3$–1.9.

Svensson [30] conducted a numerical study to investigate the streamwise and spanwise flow patterns over different rounded three-dimensional contour bumps in both subsonic, transonic and supersonic free-stream to investigate the applicability of contour bumps with various geometries in DSI. The author concluded that for a contour bump with a given bump width and apex height, the size of the wake region and the spanwise vortices that formed in the bump valley increases with increasing free-stream Mach number (M_∞) when $M_\infty < 1$. In contrast, when $M_\infty > 1$, the size of the wake region and the spanwise vortices decreases with increasing free-stream Mach number. This is agreed with the results shown by Lo [26] and Lo et al. [28,29].

It is clear that the occurrence of flow separation and the formation of the spanwise vortices increase the pressure drag generated by the bumps. In addition, when contour bumps are used in DSI, these effects lower the total pressure recovery that can be achieved and also affect the uniformity of flow entering the engines [17,30]. Therefore, effective measures must be established in order to achieve flow separation control in contour bumps. Jet blowing is one effective way to achieve flow separation control and it has been extensively investigated in the subsonic flow regime. In contrast, using continuous jet blowing in flow separation control in supersonic flow is less common. The studies conducted by Zubkov et al. [31], Glagolev et al. [32,33], Glagolev and Panov [34] and very recently Beketaeva et al. [51] were some of the earliest experimental studies to investigate the interaction between the injected sonic/supersonic jet and the supersonic free-stream. In these studies, the gaseous jet was injected from a flat plate through orifices of different sizes. Experimental data in these studies showed that complicated three-dimensional compression waves are formed upstream of the injected jet. In addition, a pair of counter-rotating horseshoe-shaped vortices appears immediately downstream of the injected jet and the tips of these horseshoe vortices propagated downstream from the jet.

One of the first experimental studies that investigated the flow physics of supersonic flow past a flying object with sonic and supersonic jet injection employed was conducted by Zubkov et al. [35]. Experimental data in [35] showed that the interaction between the injected jet and the supersonic free-stream leads to the formation of a shock wave immediately upstream of the jet. In addition, counter-rotating vortices were observed in the leeward side of the model. Koike et al. [36] found that by blowing jet continuously at the leeward face of a micro-ramp in a Mach 2.6 free-stream could reduce the extent of flow separation that occurred. The authors explained that the blowing jets reduced the size of the spanwise vortices that formed and also led to the formation of a streamwise vortex pair downstream of the micro-ramp. These streamwise vortices facilitate flow mixing between the low energy boundary layer and the high energy free-stream. As a result, the boundary layer was re-energised and thus delayed flow separation. Lo et al. [26,28] experimentally investigated flow separation control in a three-dimensional contour bump using active blowing jet in a Mach 1.3 free-stream. Similar to the conclusion obtained by Zubkov et al. [35] and Koike et al. [36], the authors found that the blowing jet hindered the formation of the spanwise vortices and also reduced the size of the wake region that appeared in the bump valley.

The present study aims to extend the previous studies conducted by Lo et al. [26,28] to a higher free-stream Mach number to simulate the working conditions of a diverterless supersonic inlet. This experimental study aims to firstly look at the flow physics of a three-dimensional rounded contour bump with and without active sonic jet blowing involved in a Mach 1.9 free-stream. Secondly, the effect of the jet total pressure in affecting the streamwise and spanwise flow patterns over the contour bump is also included in this study.

2. Experimental setup

2.1. Tri-sonic wind tunnel

All of the experiments in this campaign were conducted in an intermittent in-draught type tri-sonic wind tunnel. An intermittent in-draught type wind tunnel means that the airflow inside it is maintained by means of a pressure difference between the atmosphere (upstream) and vacuum (downstream). A schematic of this wind tunnel facility is shown in Fig. 1. The same trisonic wind tunnel was also employed in the experimental studies conducted by Lo [26], Lo and Kontis [27], Lo et al. [28,29], Zare-Behtash et al. [46,47], and Ukai et al. [48–50]. The wind tunnel has a rectangular test section with dimensions of 485.5 mm (length) × 150 mm (width) × 216 mm (height). The three-dimensional rounded contour bump model was floor mounted at the middle of the wind tunnel test section. Optical access is achieved through the two quartz side and the top windows which is also made of quartz. A quick opening butterfly valve is situated between the test section and the vacuum tank. When the butterfly valve is opened, a pressure difference is generated between the upstream of the wind tunnel and the vacuum tank. As a result, a stable airflow is developed inside the wind tunnel. The required Mach 1.9 supersonic free-stream was generated by expanding the airflow inside the wind tunnel through a pair of convergent–divergent nozzles situated upstream of the test section.

The free-stream Mach number (M_∞) at the wind tunnel test section was calculated from the total pressure ratio between the upstream and at the test section of the wind tunnel [37]. Pitot probes were inserted into the wind tunnel to obtain information about total pressures at the two different locations. The end of each pitot probe was connected to a Kulite XT-190M pressure transducer via flexible tubes. The voltage signals from the pressure transducer were captured by a National Instruments (NI)

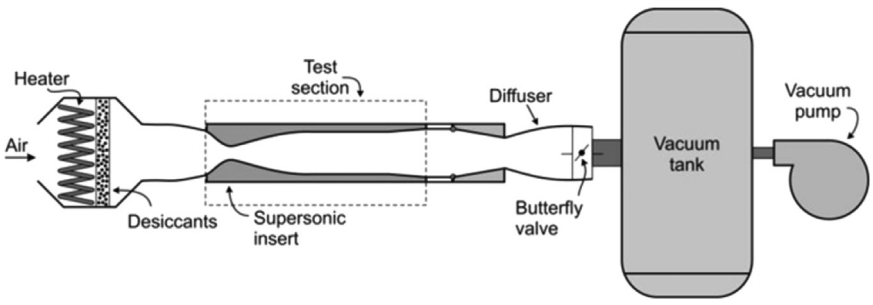

Fig. 1. Schematic of the tri-sonic wind tunnel.

NI-USB-6259 Data Acquisition (DAQ) system at a sampling rate of 20 kHz over a sampling period of 10 s. The tri-sonic wind tunnel has a stable runtime of 6 s. At $M_\infty = 1.9$, the flow Reynolds number per unit length (Re/m) is $\mathrm{Re/m} = 9 \times 10^6$ and the maximum turbulent intensity level of the free-stream is about 0.7% Under the same initial conditions, the variation of the free-stream Mach number at the test section is about $M_\infty = 1.9 \pm 0.1$.

The velocity profile of the flow measured at the location 10 mm upstream of the contour bump model is shown in Fig. 2. A turbulent flow velocity profile can be observed from Fig. 2 and the boundary layer thickness, based on 99% of the free-stream velocity (δ_{99}), is about $\delta_{99} = 8$ mm. Therefore, the boundary layer thickness is about 80% of the bump height.

2.2. Contour bump

A three-dimensional rounded contour bump model with jet orifices situated in the bump valley (hereafter referred to as the active jet bump) was used in this experimental study. The schematic of the active jet bump is shown in Fig. 3. The dimensions of the active jet bump are 75 mm (length) × 50 mm (width) × 10 mm (apex height). Three 2 mm diameter jet orifices, aligned at 45° with respect to the transverse direction, are situated in the bump valley 5 mm below the bump crest. One of these three jet orifices is located at the centreline of the bump while the other two are situated 3 mm away from the centreline in the two sides. Sonic air jet at different total pressures (P_{jet}) is blowing from these orifices in attempt to affect the flow pattern downstream of the bump crest. Totally, six different jet total pressures ranging from 0 bar (i.e. no jet) to 4 bar were used in the present study.

2.3. High-speed schlieren photography

Topler's z-type Schlieren photography technique [38,39] was employed for flow visualisation in the streamwise direction within the tri-sonic wind tunnel. The Schlieren system contains a 450 W continuous Xenon arc-lamp light source, a focusing lens, a slit with 2 mm width, a horizontal knife edge, a set of Hoya 49 mm diameter close-up lens, and two parabolic mirrors. The diameter and the focal length of each parabolic mirror are 203.2 mm and 2088 mm, respectively. It should be noted that a 5° offset angle with respect to the axis of each parabolic mirror was set to minimise the 'coma' effect. Schlieren images were captured by a Photron Fastcam SA1.1, monochrome, high-speed camera. The frame rate of the camera was set to 5000 frames per second at a resolution of 1024 pixels × 1024 pixels. The exposure time of the camera was set to 1 μs for capturing unsteadiness effects in the flow field. The schematic setup of the Schlieren photography experiments is shown in Fig. 4.

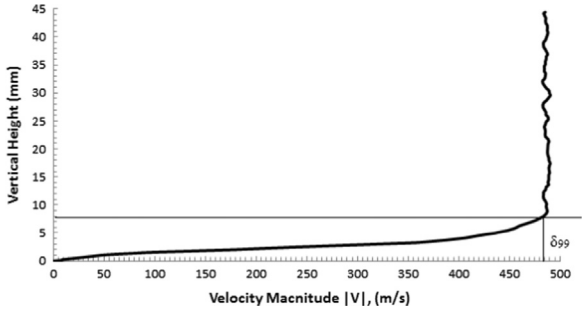

Fig. 2. Flow velocity profile in the wind tunnel at 10 mm upstream of the contour bump model.

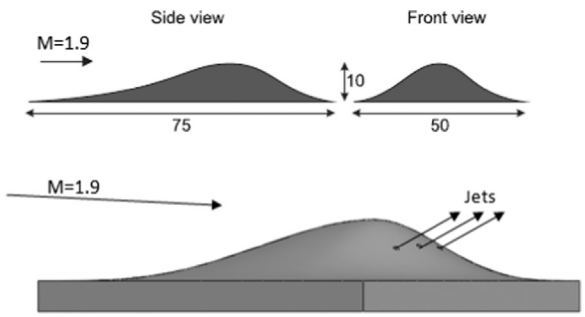

Fig. 3. Geometry of the active jet bump model.

The uncertainty of angle measurements using images obtained from the high-speed Schlieren photography experiments is calculated using Eq. (1).

$$\sigma = \sqrt{\frac{\sum_{i=1}^{n} (R_i - \bar{R})^2}{n-1}} \tag{1}$$

In Eq. (1), R_i is the angle which measured from an individual Schlieren image and $\bar{R}$ is the mean angle which is measured from n samples. Using Eq. (1), the uncertainties of the separation shock angle, shear layer angle, the reattachment shock angle and the jet-induced shock angle, based on the measurement of 200 individual Schlieren images are calculated and tabulated in Table 1.

2.4. Surface fluorescent oil flow visualisation

An in-house developed fluorescent oil recipe was used in the surface oil flow visualisation experiments. This fluorescent oil mixed from this recipe is able to follow the flow streaklines accurately in supersonic speeds [26–29,32–36]. Fig. 5 shows the schematic setup of the surface oil flow visualisation experiments.

Illumination in the surface oil flow experiments was provided by two UV LED (Light Emission Diode) panels with 225 LED units arranged in a 15 × 15 array included in each panel. These two UV LED panels were located adjacent to the two side windows to ensure the entire wind tunnel test section was uniformly illuminated. A layer of fluorescent oil of approximately 10 mm (length) × 150 mm (width) × 5 mm (thickness) was applied 100 mm upstream of the contour bump model. In order to increase contrast, the model was first sprayed with five layers of matt black acyclic paint prior to the experiments. Instantaneous oil trails along the contour bump model were captured by a ceiling mounted Cannon EOS 600D digital SLR camera which has a maximum resolution of 14 Mp. The ISO speed, shutter speed, and F-number were set to ISO400, 1/4000 s, and F11, respectively.

2.5. Particle image velocimetry

Particle Image Velocimetry (PIV) was employed to measure velocity and other flow properties along the contour bump models. The laser illumination is provided by a Litron Nano L-series, Nd:YAG Model LPU550 Q-switched double-pulsed laser. The maximum pulse energy output of the system is 200 mJ at 15 Hz repetition rate. The wavelength and the duration of the laser pulses is 532 nm and 4 ns, respectively. The laser beam generated was delivered to the wind tunnel test section via a movable laser guide arm and expanded through a series of optics to form a thin laser sheet (~0.8 mm in width). This thin laser sheet illuminated along the centerline of the contour bump model. A schematic setup of the PIV experiments is shown in Fig. 6.

The separation time between the two consecutive laser pulses (δ_t) was set to $\delta_t = 0.9$ μs. This is calculated based on the theoretically predicted flow speed of the Mach 1.9 free-stream and the size of the interrogation windows that used. Through this setting the displacement of the tracer particles between two consecutive frames was 6 pixels. Flow seeding is achieved using olive oil particles generated by

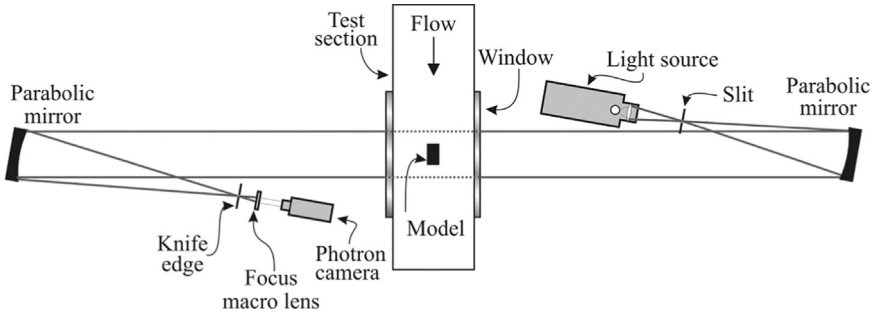

Fig. 4. Schematic of the setup of the Schlieren photography experiments.

Table 1
Estimated uncertainties in angle measurements using images obtained from high-speed Schlieren photography experiments.

Measurements	Uncertainty (deg)
Separation shock angle	± 0.5
Shear layer angle	± 0.5
Jet-induced shock angle	± 1.0
Re-attachment shock angle	± 0.5

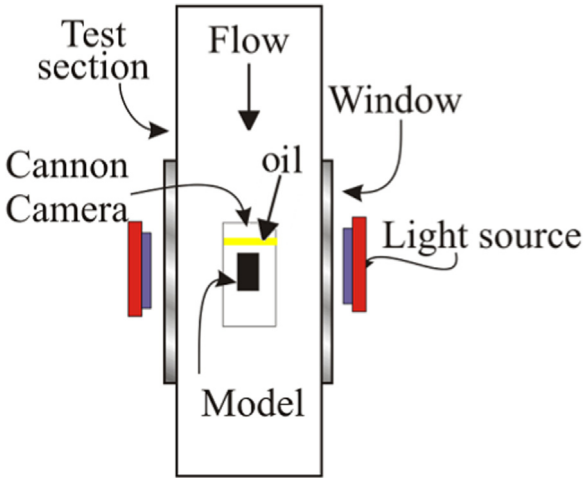

Fig. 5. Schematic of the setup of the surface oil flow visualisation experiments.

a TSI Model 9307 oil droplet generator with an aerosol flow rate of 30 L/min. The particle density (ρ_p) and diameter (d_p) are 911 kg/m^3 and 1 μm, respectively so that the corresponding Stokes number (Stk) of the seeder particles is Stk = 0.048. This ensures the seeder particles could trace the flow accurately during the measurements. PIV images were captured by a LaVision Imager Pro X 2 M CCD camera with 1600 pixels × 1200 pixels which viewed the laser sheet orthogonally. A Nikon 28 mm to 85 mm zoom lens was mounted on the camera. In addition, a 532 nm narrow band-pass filter was placed in front of the lens to minimise the background noise effects.

Approximately 80 pairs of wind-on images were recorded during each PIV measurement. Each test case was repeated at least five times to ensure the final averaged velocity vector field was constructed by averaging at least 300 image pairs. The recoded image pairs were processed by the software DaVis 7.2 using cross-correlation algorithm. Multiple stages and passes processing techniques were employed to improve the accuracy of the averaged vector field which resolved [40,50]. The PIV images were first divided into a number of 64 pixels × 64 pixels interrogation windows at which two times of cross-correlation were conducted. Then, at the second stage, the interrogation windows were refined to 32 pixels × 32 pixels and another three times of cross-correlation calculation were conducted. A 50% of overlapping between two neighbour interrogation windows was used for both stages of vector processing in order to reduce the number of spurious vectors appeared in the processed vector field.

The method used in this study to determine the uncertainty of PIV measurements was proposed and adopted by Lusk [41] and Lusk et al. [44,45]. There are three main sources of uncertainties associated with the PIV measurements. These errors include the error arises during the cross-correlation process, the accuracy of the seeder particles to follow the flow streamlines and also the uncertainty in velocity measurement using PIV. The error due to the cross-correlation analysis using the Davis 7.2 software is about 3% of the total number of vectors that are resolved by the cross-correlation algorithm [41,44]. For the accuracy of the seeder particles to follow the flow streamlines, Samimy and Lele [42] shows that the error of the seeder particles to follow the flow increases linearly with the Stokes number (Stk) when Stk < 1. Typically, when Stk = 0.2, the error of the seeder particles to follow the flow streamlines is about 2%. In the presence study, the maximum Stoke number is Stk = 0.048. Therefore, the maximum error of the seeder particles to follow the flow streamlines is 0.48%.

Grant and Owens [43] proposed a formula (Eq. (2)) to calculate the uncertainty of the velocity measurement (ε_σ) by using PIV under a turbulent flow:

$$\epsilon_\sigma = \frac{z_c}{\sqrt{2N}}\sqrt{(1 + 2T_i^2)} \tag{2}$$

In Eq. (2), N is the total number of images obtained from the PIV measurement and z_c is the confidence coefficient, T_i is the local turbulent intensity of the flow. Eq. (2) is valid when the turbulent intensity in any part of the flow is smaller than 30% [43]. For a 95% of confidence level, the corresponding confident coefficient is $z_c = 1.96$. Since at least 300 pairs of images (i.e. minimum 600 images) are used to produce a time-averaged PIV image and noting that maximum local turbulent intensity of the flow is about 8%, the maximum error in local velocity measurement (ε_σ) using PIV is about 5.6%. By combining all individual errors that occurred in the PIV measurements, the overall uncertainty of the PIV measurements is about 6.4%.

In addition, the average flow acceleration characteristic (a_{flow}) of the active jet bump with 4 bar total pressure blowing jet employed is evaluated along various normalised x-locations (i.e. x/h where h is the apex height of the contour bump). The result obtained is tabulated in Table 2.

3. Results and discussion

3.1. Surface oil flow visualisation

Fig. 7 (a)–(f) show the spanwise flow pattern over the active jet bump with jet blowing at different total pressures obtained from the surface oil flow visualisation experiments.

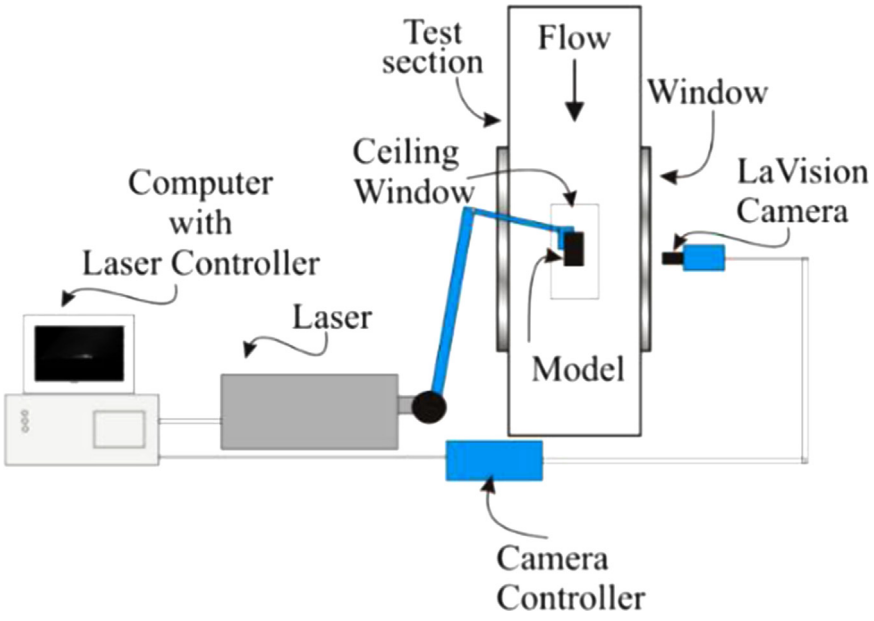

Fig. 6. Schematic of the setup of the particle image velocimetry experiments.

Table 2
Flow acceleration characteristic along various normalised x-locations (x/h) of the active jet bump with 4 bar total pressure jet blowing in the bump valley.

a_{flow} (ms^{-2})	at $x/h=0$	at $x/h=0.25$	at $x/h=0.5$	at $x/h=0.75$
4 bar jet	−3.79	6.46	−2.95	−4.31

It can be seen from Fig. 7 (a)–(f) that upstream of the bump crest the spanwise flow pattern remains similar for all cases being studied. The incoming flow was deflected upward and sideway by the ramp-shaped front surface of the active jet bump. As a result, the flow followed the contour and moved along the front part of the bump and eventually reached the bump crest. Due to the rapid change in the contour along the bump valley the flow separated downstream of the bump crest which is evidenced by the presence of a separation line (S.L.) at the bump crest.

The flow pattern along the bump valley of the active jet bump is affected by the blowing jet and cannot be generalised. In the baseline case when no jet is blowing in the bump valley (Fig. 7 (a)) two big counter-rotating spanwise vortices (V) are formed in the bump valley. It is deduced that as a result of the flow separation, a low pressure wake region is formed downstream of the bump crest. This low pressure zone attracts the relatively high pressure flow from the two sides of the bump to circulating in the bump valley which eventually leads to the formation of the spanwise vortex pair. Interesting changes appear when jet starts blowing in the valley of the active jet bump. When the total pressure of the blowing jet is set to 0.5 bar (Fig. 7 (b)), the two large spanwise vortices shown in the baseline case with no jet blowing (Fig. 7 (a)) disappear. Instead, two highly distorted spanwise vortices are formed in the upper part of the bump valley. Similar flow pattern also appears when the jet total pressure is increased to 1 bar (Fig. 7 (c)). In this case, the stronger jet further distorted the spanwise vortex pair that results in the presence of the smaller spanwise vortices in the bump valley.

Further changes appear when higher total pressure jet is used. When the total pressure of the blowing jet is set to 2 bar (Fig. 7 (d)), four mini-vortices (M.V.) are presented in the bump valley. Two of these mini-vortices are formed near the two jet orifices located at the two sides while another two are situated in the lower part of the bump valley. Similar flow pattern can also be observed once the total pressure of the blowing jet is increased to 3 bar (Fig. 7 (e)) and 4 bar (Fig. 7 (f)). From Fig. 7 (e) and (f), it can be seen that, with these two jet total pressures, the size of the two mini-vortices that situated near the jet orifices reduced significantly and they could only barely be seen. In contrast, the two mini-vortices located near the rear end of the active jet bump become bigger and more clearly defined.

To summarised, it is observed that the blowing jet can distort and reduce the size of the spanwise vortices that formed in the bump valley, particularly in those cases with high jet total pressures employed. In fact, the effects of the injected sonic jet in affecting the vortical structures that formed in the leeward side of an object in supersonic free-stream was also documented in [35]. Although a different test model was used by Zubkov et al. [35], some similarity in terms of the effects of injected jet in altering the size and formation location of the spanwise vortices can be observed from [35]. It is believed that the blowing jet increases the local pressure level in the area around the three jet orifices in the bump valley. Therefore, less flow is attracted to move to the bump valley from the two sides which eventually leads to the formation of the smaller spanwise vortices.

There is one point should be noted here. It would be useful if the pressure distributions over various cross sections of the contour bump are measured. Unfortunately, no pressure measurements were conducted due to the design constraint of the contour bump model. A gas plenum that connected with the three jet orifices is situated at the underside of the contour bump model. Therefore, it is not feasible to implement any pressure taps on the bump model as they would have to penetrate through the gas plenum that would completely change the flow pattern over the contour bump.

3.2. *Schlieren photography*

Schlieren photography images shown in Fig. 8 (a)–(f) are used to show the streamwise flow pattern along the active jet bump. Flow compression occurred when the incoming Mach 1.9 supersonic free-stream reaches the front of the active jet bump which results in the formation of a separation shock (S.S.) at the beginning of the bump. Across the separation shock, the supersonic flow follows the ramp-shaped front surface of the bump to reach the

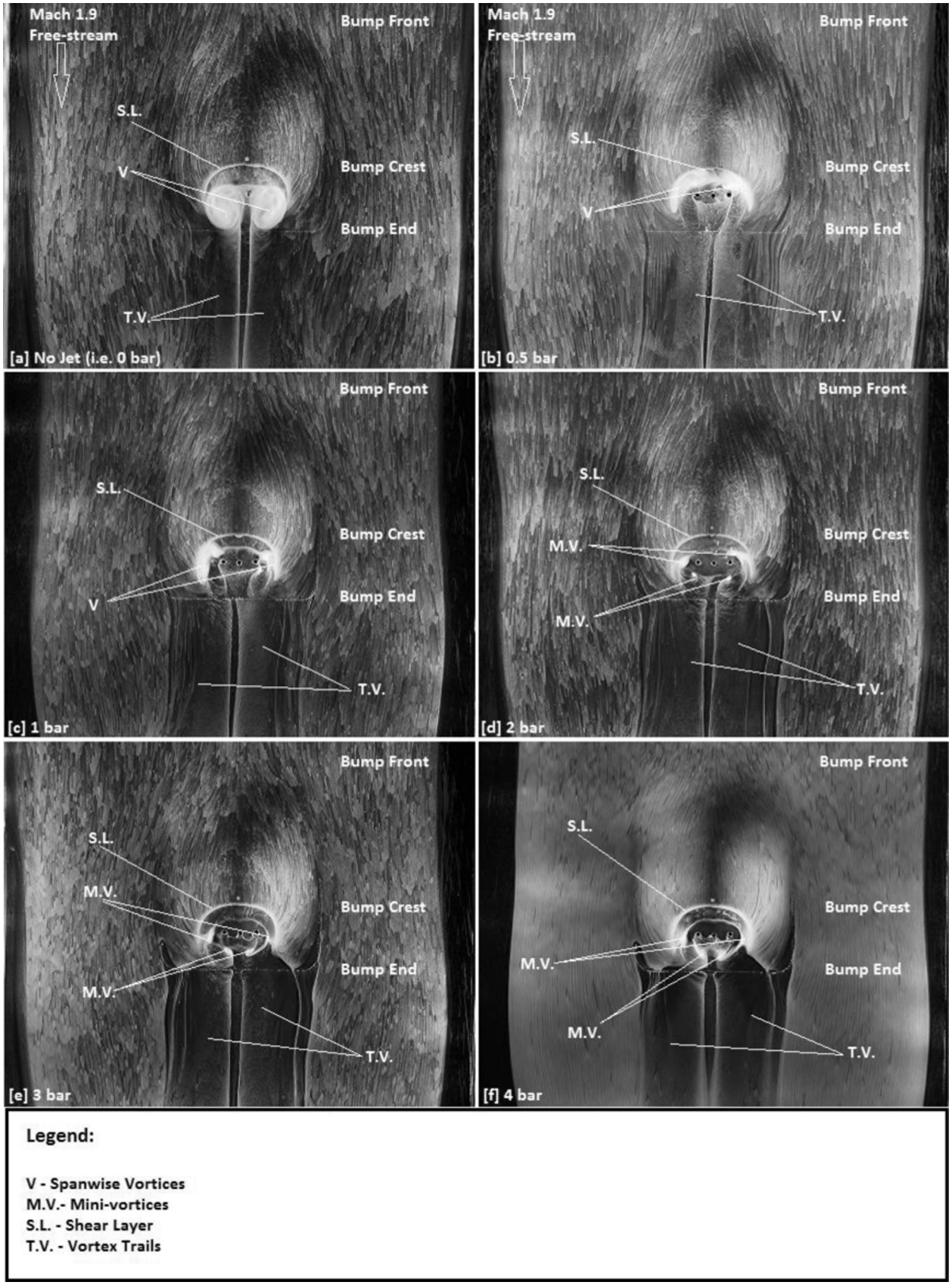

Fig. 7. Surface oil flow visualisation images of the active jet bump with: (a) no jet blowing, (b) 0.5 bar, (c) 1 bar, (d) 2 bar, (e) 3 bar, and (f) 4 bar jet total pressure.

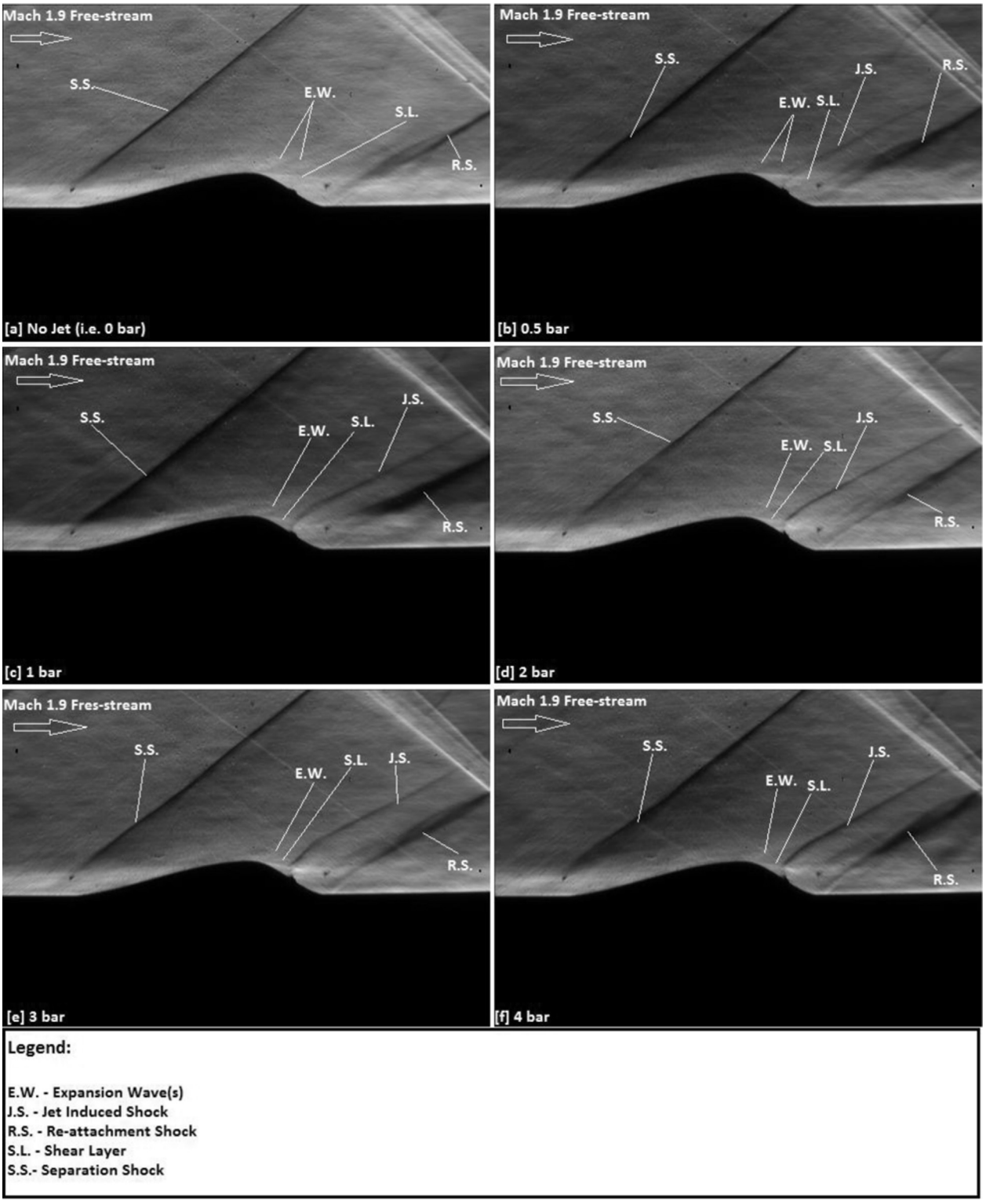

Fig. 8. Schlieren images of the active jet bump with: (a) no jet blowing (0 bar), (b) 0.5 bar, (c) 1 bar, (d) 2 bar, (e) 3 bar, and (f) 4 bar jet total pressure.

bump crest at which the flow is expanded. This is evidenced by the presence of a series of expansion waves (E.W.) around the bump crest as seen in the Schlieren images. As the flow is separated from the bump immediately downstream of the bump crest, therefore, a shear layer in formed downstream of the bump crest.

The flow pattern behind the bump crest depends on whether the blowing jet in the bump valley is being turned on. In the baseline case with no jet blowing (Fig. 8 (a)), no noticeable flow feature can be observed along the bump valley. However, in those cases with active jet blowing employed (Fig. 8 (b)–(f)), a shock wave known as the jet induced shock (J.S.) is presented adjacent to the three jet orifices in the bump valley. Its formation is due to the ramping effects induced by the blowing jet. In fact, similar conclusions and flow features appear around the injected jet were also documented and shown in Zubkov et al. [31,35], Glagolev et al. [32,33] and Glagolev and Panov [34]. Basically, immediately

upstream of the injected jet, complicated three-dimensional compression waves appear and the collision of these compression waves at a more downstream location leads to the formation of the jet induced shock. In addition, turbulent flow structures are formed immediately downstream of the injected jet. According to Zubkov et al. [31,35], Glagolev et al. [32,33] and Glagolev and Panov [34], these turbulent flow structures are actually a pair of horseshoe-shaped vortices that propagate downstream. Finally, at the rear end of the active jet bump, another shock known as the reattachment shock (R.S.) appears. Across the reattachment shock, the flow becomes parallel to the free-stream direction again.

An interesting observation should be noted here. From Fig. 8 (b)–(f), it can be seen that the shear layer seems to be deflected downward by the jet or the jet induced shock in those cases with jet blowing in the bump valley. It is evidenced by plotting the average shear layer angle ($\delta_{S.L.}$) of the active jet bump with and without jet blowing employed (Fig. 9). It should be noted that the averaged shear layer angle in each case is calculated by averaging the shear layer angle of 200 instantaneous Schlieren images. From Fig. 9, it can be seen that the shear layer angle is the largest (i.e. the least downwards) when no jet is blowing in the bump valley. Once jet blowing is activated, the shear layer angle decreases progressively when the total pressure of the blowing jet is increased from 0.5 to 2 bar. The shear layer angle is then remained relatively constant with increasing jet total pressure from 2 to 4 bar. From this it is concluded that the blowing jet could deflect the shear layer downwards which, in turn, might affect the size of the wake region that formed downstream of the bump crest.

3.3. Particle image velocimetry (PIV) measurements

Qualitative and quantitative data obtained from Particle Image Velocimetry (PIV) measurements are presented in this sub-section. The time-averaged x- and y-velocity contours along the centerline of the active jet bump with and without jet blowing employed are shown in Figs. 10 and 11, respectively. As already mentioned in subsections 3.1 and 3.2, similar flow pattern appears upstream of the bump crest of the active jet bump regardless whether the jet blowing is activated. This can be observed from Figs. 10 and 11 that similar x- and y-velocity contours are shown upstream of the bump crest in all cases being studied.

It is evidenced by plotting the normalised velocity profiles in x- and y-directions at the normalised location $x/h=3$ (i.e. at the middle of the bump front surface) where h is the apex height of the bump (Fig. 12). It should be noted that the flow velocity in x- and y-directions is normalised with the mean free-stream velocity (U_∞) where $U_\infty=487\ \mathrm{ms}^{-1}$. As very similar velocity profiles are obtained in all cases being studied as seen in Fig. 12, this indicates that the blowing jet in the bump valley does not exert any effects in affecting the flow pattern upstream of the bump crest. Although small fluctuations in the velocity profiles in different cases being studied can be observed in Fig. 12, it is believed that those fluctuations are caused by small velocity fluctuation during the wind tunnel operation and might be ignored.

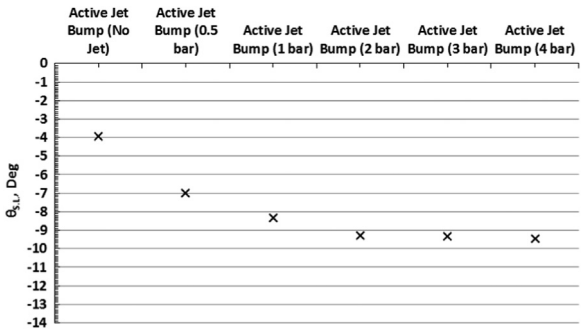

Fig. 9. Shear layer angle of the active jet bump at different jet total pressures.

In contrast, the flow pattern downstream of the bump crest is strongly influenced by the blowing jet and the total pressure of the jet. In exact, the blowing jet in the bump valley affects the shear layer angle and also the size of the wake region downstream of the bump crest. This can be confirmed by observing the x-velocity contour along the centerline of the active jet bump (Fig. 10). In the baseline case with no jet blowing is employed (Fig. 10 (a)), a long and wide low pressure region, i.e. the wake region, appears downstream of the bump crest of the active jet bump. The formation of this low pressure wake region is caused by the flow separation that happens immediately downstream of the bump crest. The length (l_{wake}) and the maximum height (h_{wake}) of the wake region are about $l_{wake}=0.53c$ and $h_{wake}=0.13c$, where c is the length of the bump. This indicates that the length of the wake region in this case is more than half of the length of the active jet bump.

However, some changes in the size of the wake region occur in those cases with jet blowing employed. In the case when the blowing jet is at 0.5 bar total pressure (Fig. 10 (b)), a considerably shorter and narrower wake region is formed in the bump valley compared to the baseline case. Quantitatively, the length and the maximum height of the wake region are $l_{wake}=0.37c$ and $h_{wake}=0.11c$, respectively. This means that the jet at 0.5 bar total pressure could reduce the size of the wake region by 41% compared to the baseline uncontrolled case. Similar results can also be observed in those cases when the total pressure of the blowing jet is set to above 0.5 bar (Fig. 10 (c)–(f)). When the total pressure of the blowing jet is at 1 bar (Fig. 10 (c)), the size of the wake region becomes marginally smaller than that when the blowing jet pressure is at 0.5 bar. In this case, the length and the maximum height of the wake region are about $l_{wake}=0.31c$ and $h_{wake}=0.11c$, respectively. This indicates that the wake region is around 51% smaller than that in the baseline case.

Significant changes occurs in the case with 2 bar total pressure jet blowing in the bump valley. As seen in Fig. 10 (d), a short and narrow wake region is formed downstream of the bump crest. In fact, the size of the wake region in this case is around $l_{wake}=0.25c$ and $h_{wake}=0.09c$ which is 67% smaller than that as seen in the baseline case. The presence of this small wake region indicates that the separated flow quickly reattached downstream of the bump crest. This implies that the extent of flow separation is significantly controlled by the 2 bar total pressure jet in the bump valley. However, the size of the wake region remains relatively constant once the total pressure of the blowing jet is increased to above 2 bar. It can be revealed by observing Fig. 10 (e) and (f) for the cases in which the total pressure of the blowing jet is at 3 and 4 bar, respectively. Quantitatively, the wake region has the size of $l_{wake}=0.26c$ and $h_{wake}=0.1c$ at 3 bar while $l_{wake}=0.24c$ and $h_{wake}=0.09c$ at 4 bar jet total pressure. This indicates that the size of the wake region in these two cases is similar to that with 2 bar total pressure jet employed as shown in Fig. 10 (d).

It is therefore clear that flow separation control in contour bumps can be achieved effectively in supersonic speeds using active jet blowing. In this study, this flow control strategy is particularly effective when the jet total pressure of the blowing jet is at 2 bar. It is deduced that the blowing jet provides two effects in achieving flow separation control. First of all, the momentum of the flow is increased by the blowing jet which accelerates the reattachment of the separated flow downstream of the bump crest. Secondly, the blowing jet seems to be able to reduce the size of the wake region which formed downstream of the bump crest by deflecting the shear layer more downwards. This is partially supported by visualising the y-velocity contour along the centerline of

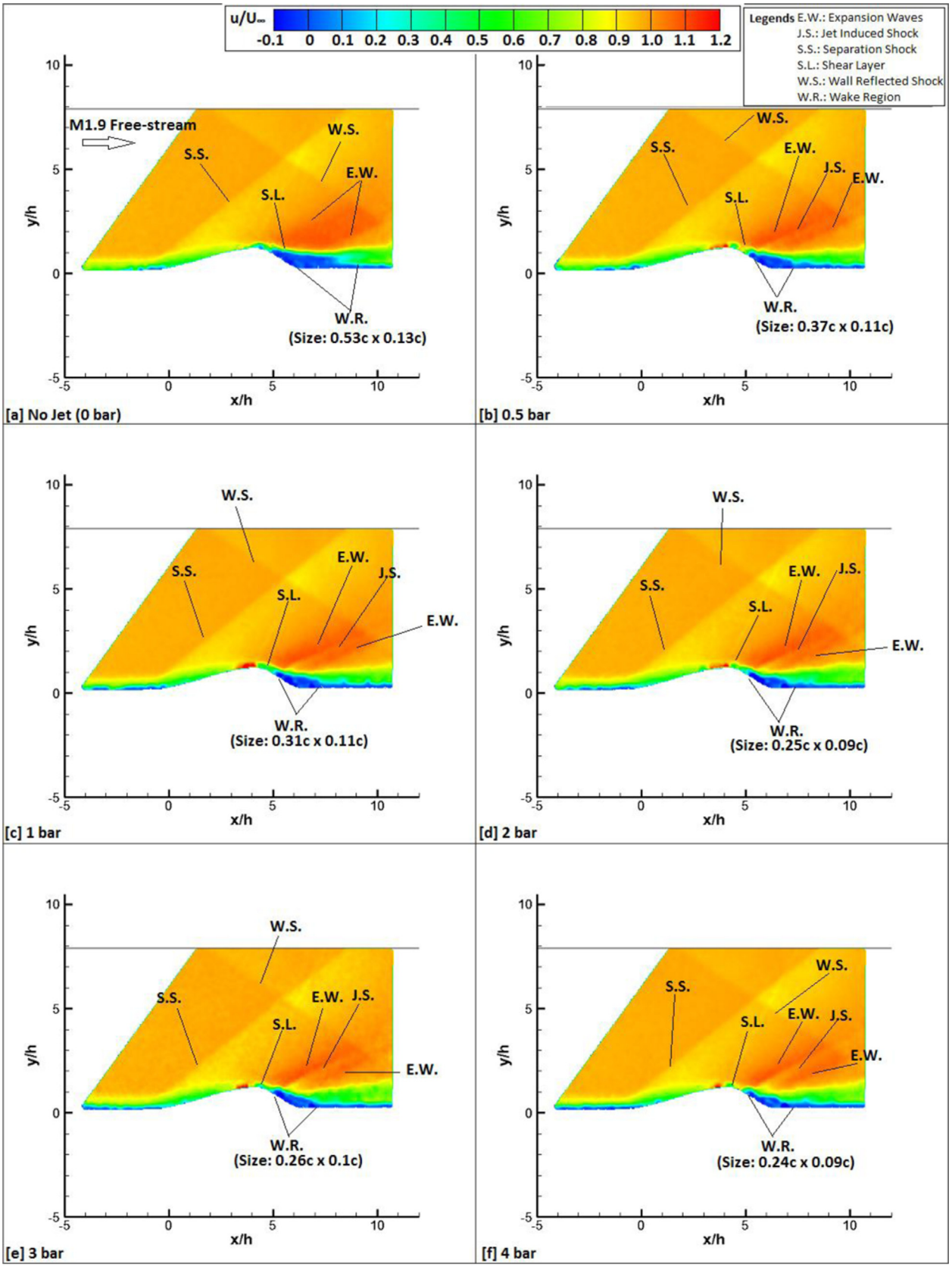

Fig. 10. The time-averaged *x*-velocity contour along the active jet bump with jet total pressure of: (a) no jet, (b) 0.5 bar, (c) 1 bar, (d) 2 bar, (e) 3 bar and (f) 4 bar.

the active jet bump shown in Fig. 11. From Fig. 11 (a) to (f), a region that shows negative *y*-velocity (i.e. downward flow movement) exists slightly downstream of the bump crest in all cases being studied. However, the size and strength of this region vary with the total pressure of the blowing jet. In the baseline case in which no jet blowing is used (Fig. 11 (a)), the region that shows negative

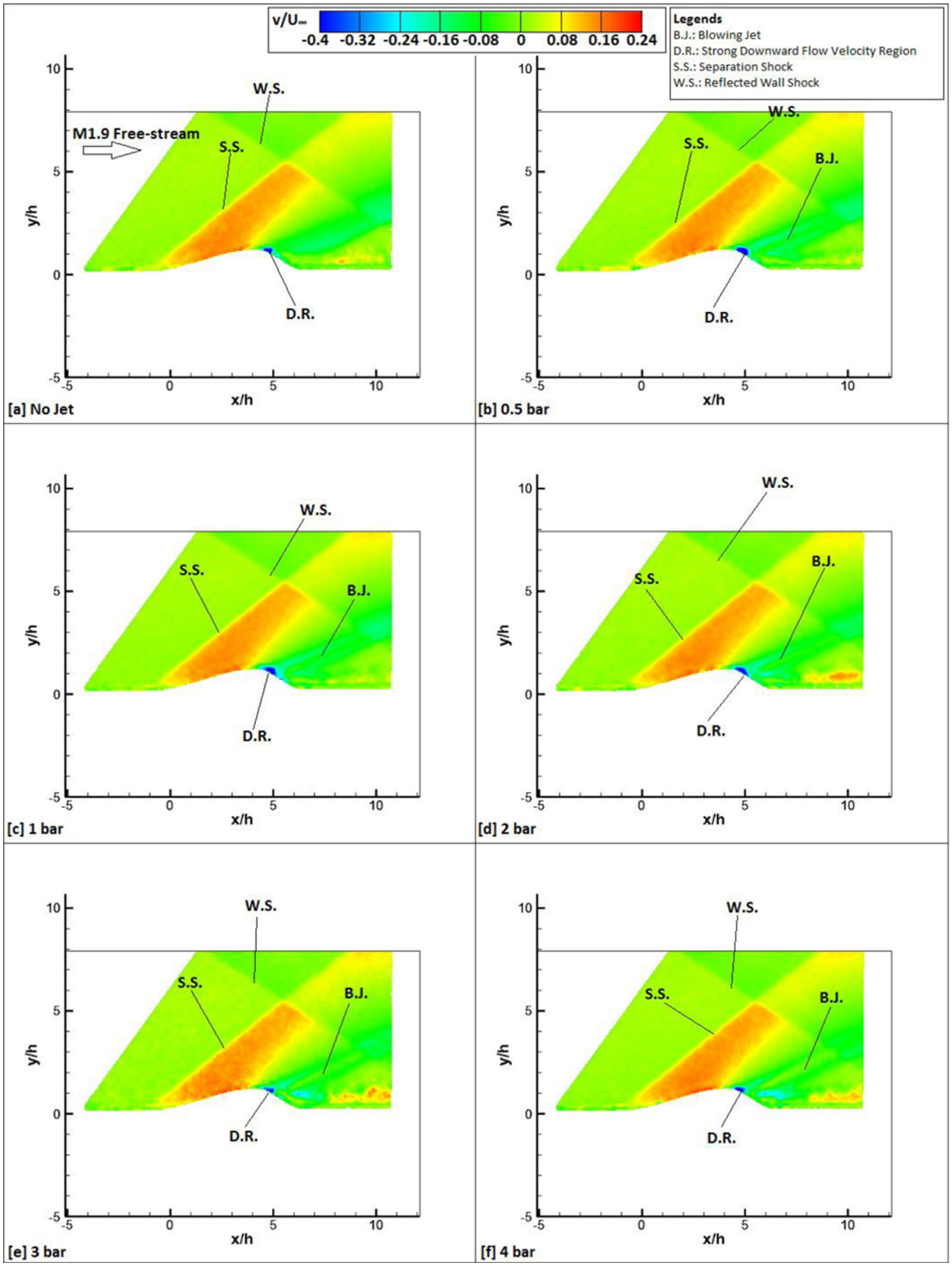

Fig. 11. The time-averaged *y*-velocity contour along the active jet bump with jet total pressure of: (a) no jet, (b) 0.5 bar, (c) 1 bar, (d) 2 bar, (e) 3 bar and (f) 4 bar.

y-velocity is considerably small.

However, once the blowing jet is activated the size of that region increases progressively with increasing jet total pressure from 0.5 to 2 bar (Fig. 11 (b)–(d)). This indicates that the flow shows progressively stronger downward movement downstream of the bump crest which, in turn, leads to the formation of progressively

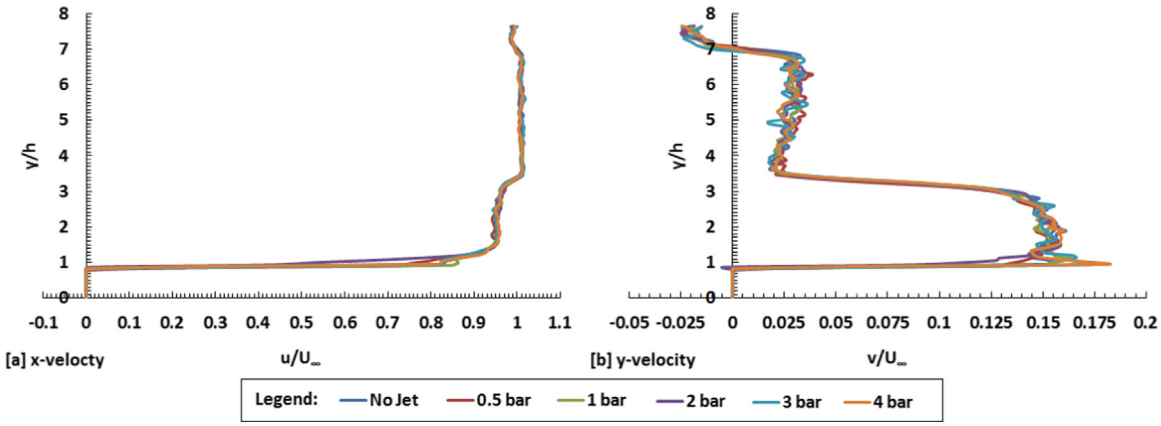

Fig. 12. The normalised velocity profiles in x- and y-directions of the active jet bump with different jet total pressures at the normalised location $x/h=3$ (i.e. middle of the bump front surface).

smaller wake region. Interestingly, once the total pressure of the blowing jet increased further to 3–4 bar (Fig. 11 (e) and (f)), the region that shows downward flow movement becomes similar to that as seen in the baseline case (Fig. 11 (a)). However, stronger downward flow movement is shown downstream of the bump crest in these cases. This is evidenced by considering the normalised y-velocity profiles of the flow (v/U_∞) at the normalised locations $x/h=6$ to 8 (Fig. 13), i.e. the wake region that presence downstream of the bump crest, for the cases with jet total pressure set to 2–4 bar. In general, the flow shows progressively stronger downward motion at the normalised locations $x/h=6$ and 7 with increasing jet total pressure from 2 to 4 bar. This explains why the wake region remains relatively constant in size once the jet total pressure is above 2 bar although a smaller region which shows downward flow motion exists.

Time-averaged z-vorticity contour shown in Fig. 14 is used to investigate the steadiness of the flow along the active jet bump with and without jet blowing employed. In the baseline case (Fig. 14 (a)), the flow immediately downstream of the bump crest is highly rotational resulting from the flow separation that happens there. This is evidenced by the presence of a region that shows relatively high negative z-vorticity downstream of the bump crest. However, once the blowing jet in the bump valley is activated (Fig. 14 (b)–(f)), the flow immediately downstream of the bump crest becomes less rotational. It is believed that the blowing jet stabilised the separated flow by increasing its momentum. In addition, from Fig. 14 (a)–(f), it can be seen that in all cases being studied, a region which shows high levels of positive z-vorticity appears in the bump valley. This is due to the presence of the wake region resulting from the flow separation downstream of the bump crest. However, as seen in Fig. 14, the size of the region which shows high levels of positive z-vorticity becomes progressively smaller when the total pressure of the blowing jet increases progressively from 0 bar (Fig. 14 (a)) to 2 bar (Fig. 14 (d)) and remains relatively constant afterwards. This result further confirmed that blowing jet in the bump valley could effectively achieve flow separation control in contour bumps in supersonic speeds.

4. Conclusions

This study experimentally investigated the flow patterns of the active jets bump with and without jet blowing in the bump valley. The jet total pressure employed was in the range of 0 bar (i.e. no jet) to 4 bar. Surface oil flow visualisation, Schlieren photography technique and particle image velocimetry measurements were used for flow visualisation and diagnostics. Results obtained from the surface oil flow visualisation experiments suggested that the blowing jet could distort the spanwise vortices that formed in the bump valley. In addition, it was observed that the blowing jet could reduce the size of the spanwise vortices. It is believed that the jet increases the local pressure level, thus hindered the formation of the spanwise vortices at the centre portion of the bump valley. Also, it was found that high total pressure jet is more effective is reducing the size of the spanwise vortices in the bump valley. It is deduced that a high total pressure jet exerts effect to a large area in the bump valley, thus making the formation of the spanwise vortices becomes more difficult.

From the Schlieren photography images, it was observed that the blowing jet does not exert any upstream effects to the flow. However, the interaction between the blowing jet and the flow downstream of the bump crest leads to the formation of the jet induced shock in the bump valley. It is believed that the jet induced shock or the blowing jet could deflect the shear layer downwards such that it could affect the size of the wake region in the bump valley. In fact, by measuring the average angle of the shear layer for the active jet bump with different jet total pressure employed, it was observed the shear layer angle becomes more negative (i.e. shows stronger downward movement) when the total pressure of the blowing jet is increased from 0 (i.e. no jet) to 2 bar. However, further increase the total pressure of the blowing jet to above 2 bar exerts no significant influence in further chaining the shear layer angle.

From the results obtained from the PIV measurements, it was concluded that the blowing jet in the bump valley could effectively reduce the extent of flow separation appears downstream of the bump crest. It was observed that the size of the wake region became progressively smaller when the blowing jet total pressure was progressively increased from 0 to 2 bar and remained relatively constant afterwards. In the case when the total pressure of the blowing jet is at 2 bar, the size of the wake region is about 67% smaller than that as seen in the baseline case in which no jet blowing is employed in the bump valley. It is believed that the blowing jet increases the momentum of the separated flow downstream of the bump crest as well as the blowing jet deflects the shear layer downwards. It is deduced that the combination of

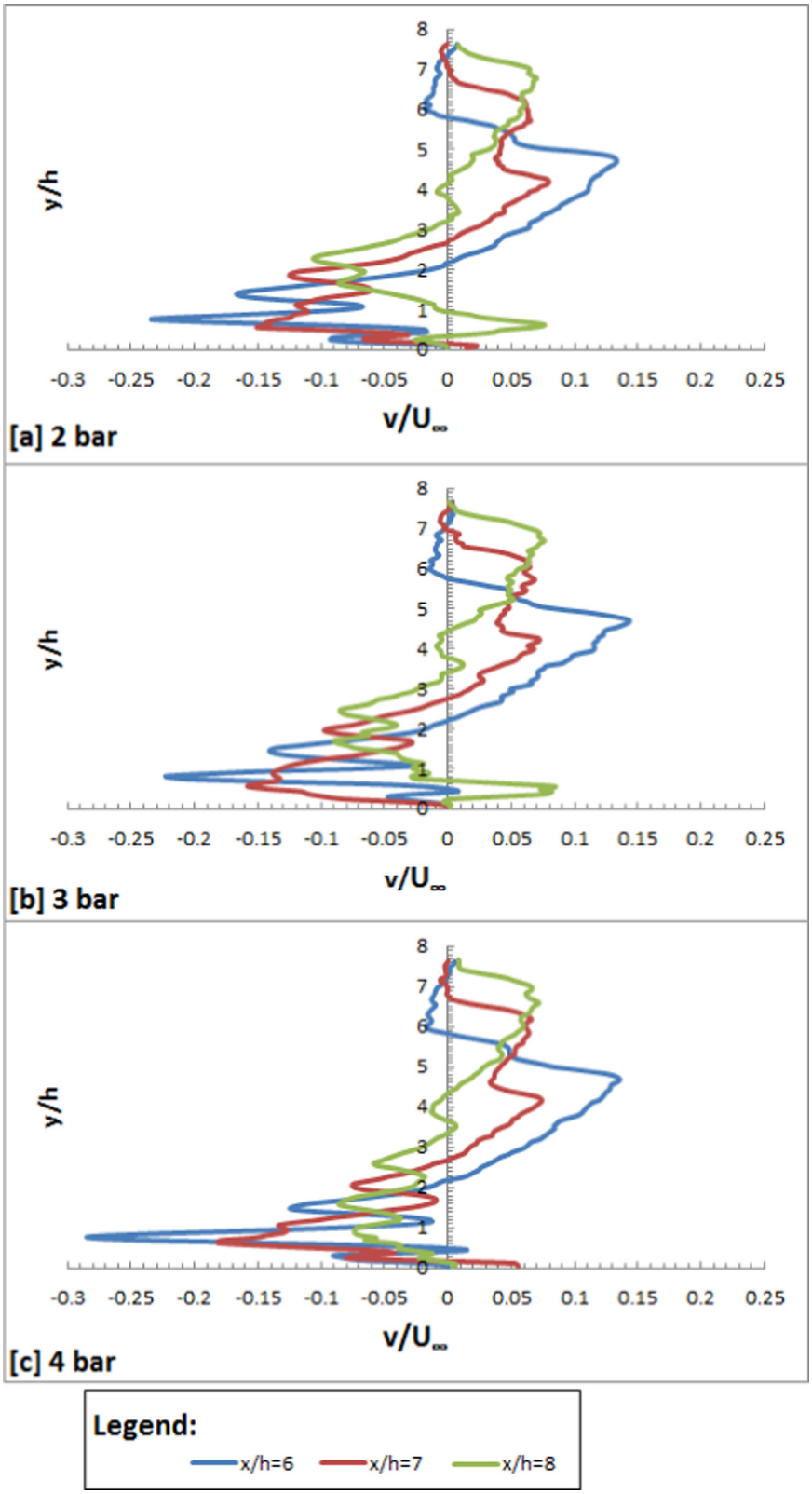

Fig. 13. The normalised *y*-velocities of the flow at the normalised locations $x/h=6$, 7 and 8 (i.e. in the wake region of the model) of the active jet bump with (a) 2 bar, (b) 3 bar and (c) 4 bar jet total pressure.

these two effects lead to the quick reattachment of the separated flow downstream of the bump crest which eventually reduces the size of the wake region.

Finally, it was concluded from the *z*-vorticity contour plots that the flow downstream of the bump crest shows lower vorticity when jet is blowing in the valley of the active jet bump compared to the baseline case. This, in turns, indicated that the blowing jet in the bump valley could increase the steadiness of the flow downstream of the bump crest of the active jet bump, particularly when the blowing jet has high total pressure. This is believed to be due

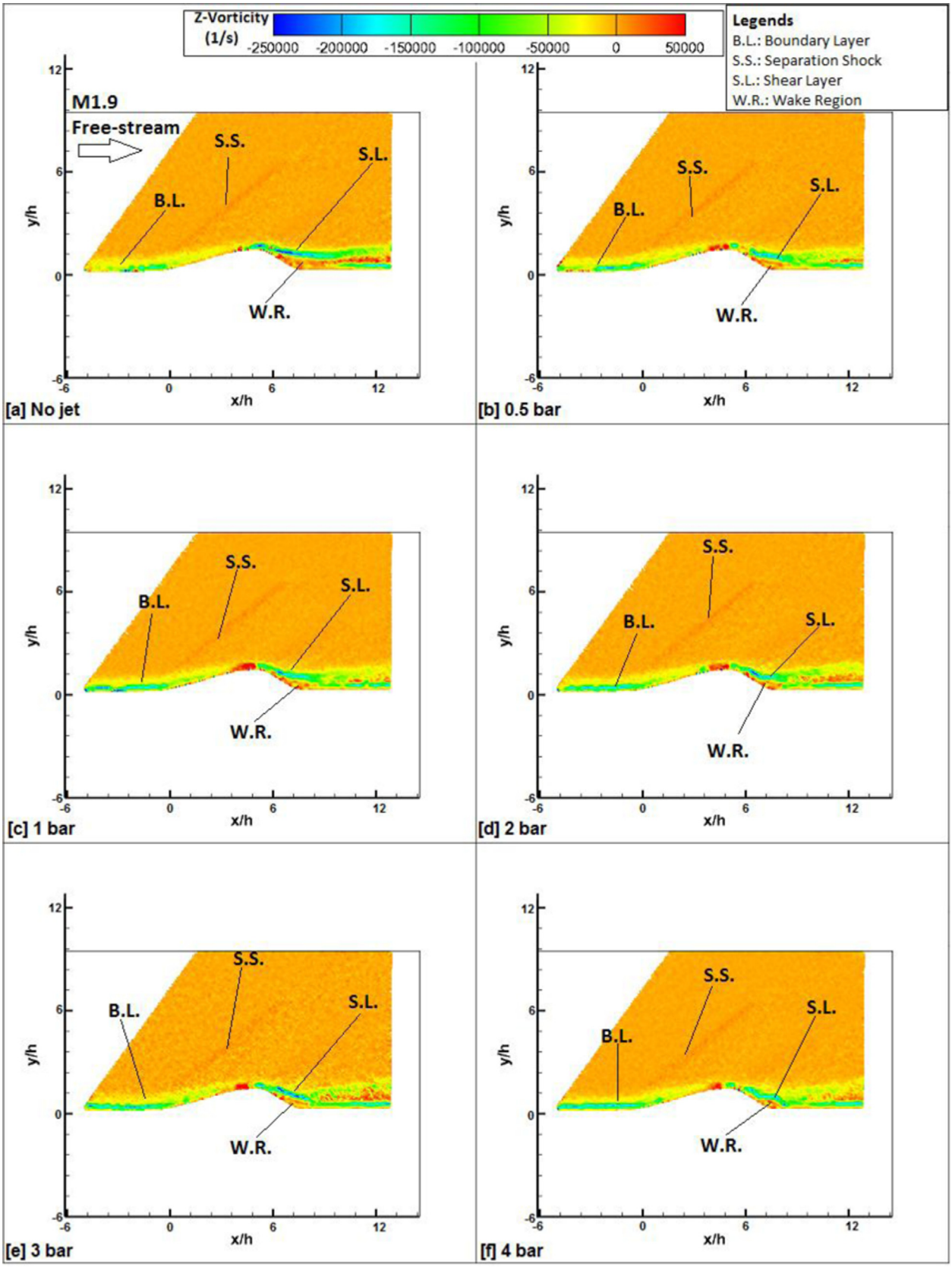

Fig. 14. The time-averaged *z*-vorticity contour along the active jet bump with jet total pressure of: (a) no jet, (b) 0.5 bar, (c) 1 bar, (d) 2 bar, (e) 3 bar and (f) 4 bar.

to the blowing jet in the bump valley increases the momentum and thus, stabilised the flow downstream of the bump crest of the active jet bump.

Author contributions

Kin Hing Lo: Experimental Campaign, data analysis and

manuscript preparation. Hossein Zare-Behtash and Kostas Kontis are project supervisors.

Conflicts of Interest

The authors declare no conflict of interest.

Acknowledgements

The authors would like to acknowledge the EPSRC (Grant number: EPSRC iCASE/DSTL/MBDA 12440107) for funding this research project. In addition, the authors also would like to acknowledge the EPSRC loan pool for the Photon FastCam SA1.1 monochrome camera used in this experimental study.

References

[1] M. Kutzbach, T. Lutz, S. Wagner, Investigations on shock control bumps for infinite swept wings, in: Proceedings of the 2nd AIAA Flow Control Conference, Portland, Orlando, June 27–July 1, 2004.
[2] N. Qin, W.S. Wong, A. Le Moigne, Three-dimensional Contour Bumps for Transonic Wing Drag Reduction, Proc. I MECH E Part G J. Aerosp. Eng. 222 (5) (2008) 619–629.
[3] B. Konig, M. Patzold, T. Lutz, E. Kramer, H. Rosemann, K. Richter, H. Uhlemann, Numerical and experimental validation of three-dimensional shock control bumps, J. Aircr. 46 (2) (2009) 675–682.
[4] P.R. Ashill, J. L. Fulker, A. Shires, A novel technique for controlling shock strength of laminar flow aerofoil sections, in: Proceedings of the First European Symposium on Laminar Flow, Hamburg, March 1992.
[5] J. Birkemeyer, H. Rosemann, E. Stanewsky, Shock control on a swept wing, Journal. Aerosp. Sci. Technol. 4 (3) (2000) 147–156.
[6] G. Liu, Y. Tao, Q. Guo, Y. Sun, Transonic drag reduction with contour bump on a supercritical airfoil, in: Proceeding of the Second International Conference on Intelligent Systems Design and Engineering Application, Sanya, Hainan, January 6–7, 2012.
[7] M. Patzold, T. Lutz, T. Kramer, S. Wagner, Numerical optimisation of finite shock control bump, in: Proceedings of the 44th AIAA Aerospace Sciences Meeting and Exhibition, Reno, Nevada, United States, January 9–12, 2006.
[8] B. König, M. Pätzold, t. Lutz, E. Krämer, Shock Control Bumps on Flexible and Trimmed Transport Aircraft in Transonic Flow, New Results in Numerical and Experimental Fluid Mechanics VI, Notes on Numerical Fluid Mechanics and Multidisciplinary Design (NNFM), vol. 96, 2007, pp. 80–87.
[9] W.E. Miholen II, L.R. Owen, On the application of contour bumps for transonic drag reduction (invited), AIAA Pap. (2005) 2005-0462.
[10] R. Duvigneau, P. Chandrashekar, Kriging-based optimisation applied to flow control, Int. J. Numer. Methods Fluids 69 (11) (2012) 1701–1714.
[11] D.S. Lee, G. Bugeda, J. Periaux, E. Onate, Robust active shock control bump design optimization using hybrid parallel MOGA, Comput. Fluids 80 (2013) 214–224.
[12] H. Ogawa, H. Babinsky, M. Patzold, T. Lutz, Shock-wave/boundary-layer interaction control using three-dimensional bumps for transonic wings, AIAA J. 46 (6) (2008) 1442–1452.
[13] H. Rosemann, K. Richter, J. Birkemeyer, A.-M. Rodde, V. Schmitt, Application of a 3D shock control bump on a transport aircraft configuration, in: Proceedings of ONERA-DLR Congress, June 2003.
[14] Y. Yang, X. Liu, S. Asif, Transonic drag reduction on supercritical wing section using shock control bumps, Trans. Nanjing Univ. Aeronaut. Astronaut. 29 (3) (2012).
[15] P.C. Simon, D.W. Brown, R.G. Huff, Performance of External-Compression Bump Inlet at Mach Numbers of 1.5 and 2.0, NACA Report, NACA-RM-E56L19, 1957.
[16] W. Xie, R. Guo, A ventral diverterless high offset S-shaped inlet at transonic speeds, Chin. J. Aeronaut. 21 (3) (2008) 207–214.
[17] J. Masud, F. Akram, Flow field and performance analysis of an integrated diverterless supersonic inlet, in: Proceedings of the 48th AIAA Aerospace Sciences Meeting Including the New Horizons Forum and Aerospace Exposition, Orlando, Florida, United States, January 4–7, 2010.
[18] Y.K. Yang, Research of bump inlet design and test, Acta Aerodyn. Sinica 25 (3) (2007) 336–338.
[19] B. Tillotson, E. Loth, J. Dutton, J. Mace, B. Haeffele, Experimental study of a Mach 3 bump-compression flowfield, J. Propuls. Power 25 (3) (2009) 545–554.
[20] Y.C. Zhong, S.Z. Yu, Q. Wu, Research of bump inlet (DSI) model design and its aerodynamic properties, J. Aerosp. Power 20 (5) (2005) 740–745.
[21] P. Wooden, Use of CFD in developing the JSF F-35 outer mold lines, in: Proceedings of the 24th AIAA Applied Aerodynamics Conference, San Francisco, California, United States, June 5–8, 2006.
[22] G. Byun PhD thesis, Structure of Three-dimensional Separated Flow on Symmetric Bumps, Virginia Polytechnic Institute and State University, Blacksburg, Virginia, 2005.
[23] G. Byun, C. Long, R. Simpson, Study of vortical separation from three-dimensional symmetric bumps, AIAA Journal. 42 (4) (2004) 754–765.
[24] A. Yakeno, S. Kawai, T. Nonomura, K. Fujii, Separation control based on turbulence transition around a two-dimensional hump at different Reynolds numbers, Int. J. Heat Fluid Flow 55 (2015) 52–64.
[25] G. Iaccarino, C. Marongiu, P. Catalano, M. Amato, RANS simulation of the separated flow over a bump with active control, Annual Research Briefs, Centre for Turbulence Research, 2003, pp. 389–397.
[26] K.H. Lo PhD thesis, Experimental Studies on Contour Bumps and Cavities at Supersonic Speed, University of Manchester, Manchester, United Kingdom, 2014.
[27] K.H. Lo, K. Kontis, Flow physics of a three-dimensional rounded contour bump in a Mach 1.3 supersonic free-stream, in: Proceedings of AIAA Aviation 2015, Dallas, Texas, United States, June 22–26, 2015.
[28] K.H. Lo, H. Zare-Behtash, K. Kontis, Flow characteristics along an active jets equipped contour bump in a supersonic freestream and its potential to be applied on transonic aircraft for drag reduction: an experimental study, in: Proceedings of the 53rd AIAA Aerospace Sciences Meeting Kissimmee, Florida, January, 5–9, 2015.
[29] K.H. Lo, H. Zare-Behtash, M. Johnson, K. Kontis, Control of flow separation on a contour bump by jets: an experimental study. in: Proceedings of the 29th International Symposium on Shock Waves, Madison, United States, July 14–19, 2013.
[30] M. Svensson, A CFD Investigation of a Generic Bump and its Application to a Diverterless Supersonic Inlet, Linkopings Universitet, Master Thesis, Linkoping, Sweden, 2013.
[31] A.I. Zubkov, A.I. Glagolev, Yu. A. Panov, J.S. Hopkins, Discharge of gas jets into a supersonic stream from orifices in the lateral surface of a body, Technical Report, Defense Technical Information Center, Feb 1969, pp. 1–15.
[32] A.I. Glagolev, A.I. Zubkov, Yu. A. Panov, Supersonic flow past a gas jet obstacle emerging from a plate, Fluid Dyn. 2 (1967) 60–64.
[33] A.I. Glagolev, A.I. Zubkov, Yu. A. Panov, Interaction between a supersonic flow and gas issuing from a hole in a plate, Fluid Dyn. 3 (1968) 65–67.
[34] A.I. Glagolev, Yu. A. Panov, Interaction of a sonic boundary-layer counter-jet with a supersonic flow, Fluid Dyn. 12 (1977) 795–798.
[35] A.I. Zubkov, A.I. Glagolev, Yu. A. Panov, Injection of gaseous jets in supersonic flow from orifices located on a side wall of a flying body, Mosc. Univ. Mech. Bull., Ser. 1 Math., Mech. No 5 (1968) 66–72.
[36] S. Koike, K. Suzuki, E. Kitamura, M. Hirota, K. Takita, G. Masuya, M. Matsumoto, Measurement of vortices and shock waves produced by ramp and twin jets, J. Propuls. Power 22 (2006) 1059–1067.
[37] A. Pope, K.L. Goin, in: Robert E. Krieger (Ed.), High-speed Wind Tunnel Testing. Huntington, Publishing Company, New York, 1978.
[38] G.S. Settles, Schlieren and Shadowgraph Techniques, Springer Verlag, New York, 2001.
[39] L. Yang, H. Zare-Behtash, E. Erdem, K. Kontis, Application of AA-PSP to hypersonic flows: the double ramp model, Sens. Actuators B: Chem. 161 (2012) 100–107.
[40] J.W. Bradley, J.S. Oh, O.T. Olabanji, C. Hale, R. Mariani, K. Kontis, Schlieren photography of the outflow from a plasma jet, IEEE Trans. Plasma Sci. 39 (11) (2011) 2312–2313.
[41] W.T. Lusk, Control of Supersonic Cavity Flow by Leading Edge Blowing, University of Florida, United States, 2011, Master thesis.
[42] M. Samimy, S.K. Lele, Motion of particles with inertia in a compressible free shear layer, Phys. Fluids 3 (1991) 1915–1923.
[43] I. Grant, E.H. Owens, Confidence interval estimates in PIV measurements of turbulent flows, Appl. Opt. 29 (10) (1990) 1400–1402.
[44] T. Lusk, J. Dudley, L. Ukeiley, L. Cattafesta, flow field effects on control on supersonic open cavities, in: Proceedings of the 49th AIAA Aerospace Sciences Meeting Including the New Horizons Forum and Aerospace Exposition, Orlando, Florida, United States, 4–7 January, 2011.
[45] T. Lusk, L. Cattafesta, L. Ukeiley, Leading edge slot blowing on an open cavity in supersonic flow, Exp. Fluid 53 (2012) 187–199.
[46] H. Zare-Behtash, K.H. Lo, K. Kontis, T. Ukai, S. Obayashi, Transverse jet-cavity interactions with the influence of an impinging shock, Int. J. Heat Fluid Flow 53 (2015) 146–155.
[47] H. Zare-Behtash, K.H. Lo, L. Yang, K. Kontis, Pressure sensitive paint measurements at high Mach numbers, Flow Meas. Instrum. (2016), In press.
[48] H. Zare-Behtash, K.H. Lo, T. Ukai, K. Kontis, S. Obayashi, Experimental investigation of impinging shock-cavity interactions with upstream transverse jet injection, Trans. Jpn. Soc. Aeronaut. Space Sci. Aerosp. Technol. Jpn. 12 (ists29) (2014) 57–62, http://dx.doi.org/10.2322/tastj.12.Pe_57.
[49] T. Ukai, H. Zare-Behtash, E. Erdem, K.H. Lo, K. Kontis, S. Obayashi, Effectiveness of jet location on mixing characteristics inside a cavity in supersonic flow, Exp. Therm. Fluid Sci. 52 (2014) 59–67.
[50] T. Ukai, H. Zare-Behtash, K.H. Lo, K. Kontis, S. Obayashi, Effectiveness of dual jets distance on mixing characteristics and flow path within a cavity in supersonic cross flow, Int. J. Heat Fluid Flow 50 (2014) 254–262.
[51] A.O. Beketaeva, P. Bruel, A. Zh Naimanova, Vortical structures behind a transverse jet in a supersonic flow at high jet to crossflow pressure ratios, J. Appl. Mech. Tech. Phys. 56 (2015) 777–788.